

Fatigue Failure Analysis for Bimetallic Work Roll in Hot Strip Mills

Mohd Radzi Aridi, Nao-Aki Noda,* Yoshikazu Sano, Kakeru Takata, and Zifeng Sun

In hot rolling of steels, bimetallic rolls consisting of high-speed steel and ductile casting iron are extensively used because of their excellent hardness and wear resistance although the fatigue failure study is not available. To extend the roll life service, herein, a 3D finite element method is applied to investigate the residual stress and the rolling stress of the bimetallic work roll in the four-high rolling mill. The residual stress is analyzed by considering preheating, quenching, and tempering. Using the results as an initial condition, the rolling stress analysis is carried out consecutively. Then, the fatigue failure risk is discussed focusing on several critical points subjected to the largest stress amplitude inside of the work roll. The accuracy of the simple superposition method is also discussed to evaluate the risk conveniently.

damaged roll surface during the use until the threshold roll diameter. Compared with the backup rolls, the work roll surface is more frequently ground to remove the surface roughness caused by the wear. For this reason, in works rolls, the surface spalling hardly occurs because the fatigue cracks initiated at the roll surface are usually removed. However, the inner layer of the bimetallic roll is consecutively used and subjected to a large number of load repetitions exceeding 10^7 times corresponding to the total life of the roll. Small defects and abnormal microstructures appearing at the casting process may cause delamination of the boundary layer due to the

repeated rolling loads.^[19,20]

The previous roll failure studies mainly focused on surface failure, so-called spalling, which is mainly caused by the shearing stress due to the rolling contact fatigue at several mm depth from the roll surface.^[21–29] Compared with the spalling at the roll surface, few studies are available for the HSS/DCI boundary failure in the inner layer of work rolls. Some studies discussed the fatigue crack initiation at the internal layer without discussing the rolling normal stress σ_r causing this boundary failure.^[19,20]

Therefore, in this article, the 3D elastic–plastic contact finite element method (FEM) is applied to evaluate the rolling stress generated during rolling in a four-high rolling mill. In our recent studies, the residual stress was discussed by analyzing quenching and tempering as the appropriate compressive residual stress prevents thermal cracking at the roll surface.^[30–33] In this article, therefore, after analyzing the residual stress, the rolling stress σ_r will be clarified by applying the rolling analysis where the work roll and the backup roll are subjected to the total rolling force P_{total} as shown in Figure 1.^[34,35] Then, the risk of internal fatigue fracture will be discussed by considering the fatigue of the roll material by focusing on some critical points empirically known. As the consecutive FEM analysis considering each roll rotation is time-consuming, the simple evaluation method will be discussed by superposing the residual stress and the rolling stress.

1. Introduction

In metalworking, rolling processes are more tonnage than any other manufacturing process. Rolling technology is developing and advancing further although seemingly mature.^[1–13]


Figure 1 shows the rolling roll in roughing stands of hot rolling stand mills. By replacing the conventional single-material rolls, bimetallic work rolls are developed through improving wear resistance and heat crack resistance.^[14–16] To express the high-speed steel (HSS)/ductile casting iron (DCI) rolls, several technical words such as bimetallic, composite, and compound are commonly used. In this article, “bimetallic” has been used similarly to our previous papers. Fracture toughness is required at the roll center, whereas wear resistance and heat resistance are required at the roll surface.^[17]

Bimetallic rolls are manufactured using the centrifugal casting method where HSS is used as the outer layer and DCI is used as the inner layer.^[18] In this article, “the outer layer” is used to represent the whole outer region outside the HSS/DCI boundary. And, “the inner layer” is used to represent the whole inner region inside the HSS/DCI boundary. The bimetallic roll can be used more than 10 times longer than the high alloy grain rolls and high chromium rolls previously used. The outer layer of the bimetallic roll can be used repeatedly after removing the

2. Analysis Method

In this study, the roll residual stress is considered as an initial condition. Then, the rolling stress analysis is carried out. As the detail of the residual stress analysis is indicated in the previous paper,^[30–33] this section mainly focuses on the method of rolling stress analysis. In this study, the fatigue of the work roll is focused as the fatigue failure of the backup roll hardly happens.

M. R. Aridi, N.-A. Noda, Y. Sano, K. Takata, Z. Sun
Mechanical Engineering Department
Kyushu Institute of Technology
1-1 Sensui-cho, Tobata-ku, Kitakyushu-city 804-8850, Japan
E-mail: noda.naoaki844@mail.kyutech.jp

 The ORCID identification number(s) for the author(s) of this article can be found under <https://doi.org/10.1002/srin.202100313>.

DOI: 10.1002/srin.202100313

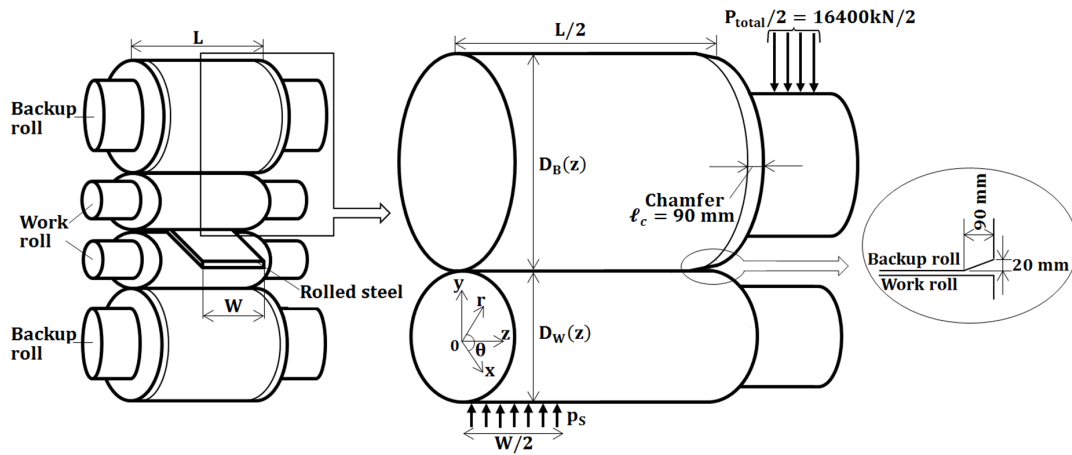


Figure 1. Schematic illustration for hot strip work roll and 3D model in four-high rolling mill.

The backup roll material is close to bearing steel and resistant to wear and fatigue. Also, the backup roll surface is occasionally ground to remove wear and fatigue layers.

Table 1 shows the roll dimensions used in the analysis. As shown in Figure 1, in this study, the following dimensions are considered; the work roll diameter $D_W = 660$ mm, the backup roll diameter $D_B = 1400$ mm, and the body length for both rolls $L = 1800$ mm and the rolled steel width $W = 1200$ mm. The width $W = 1200$ mm is commonly used and being recognized as a typical condition by many roll makers and steel companies. The work roll as well as the backup roll are subjected to the total rolling force P_{total} whose standard value is $P_{total} = 16400$ kN.^[34,35] Then, the work roll is subjected to the line force $p_S = P_{total}/W$ from the rolled steel. Also, the work roll is subjected to the line force $p_B = P_{total}/L$ from the backup roll.

As shown in Figure 1, the rolling stress of the work roll is affected by the roll profiles.^[36–41] These roll profiles include the backup roll's chamfer, the backup roll's crown, and the work roll's wear profile. Among a typical seven-stand hot strip finishing mill in steel industry, this article considers No. 4 finishing stand where the roll is used under the most severe conditions causing relatively larger wear appears and fatigue failure may happen. The previous studies showed that during one roll rotation, the thermal stress appears due to the heating and cooling of the hot plate (rolled steel) affecting only a few μm to 1 mm depth from the surface and does not affect the stress near the boundary.^[42–44] After the rolling starts, the roll temperature increases

and become stable after 1 h and reaches an equilibrium temperature of about $50\text{--}80$ °C.^[19,45] Therefore, the effect of the thermal stress can be ignored when considering fatigue fracture in this study, and the analysis is performed at room temperature.

Figure 2 shows the backup roll's crown profile with $h_c = 0.5$ mm and the work roll's wear profile with $h_w = 0.2$ mm. In this analysis, Equation (1) is assumed to express the backup roll's crown and Equation (2) is assumed to express the work roll's wear crown. The length of the curved part of the work roll is denoted as ℓ_a and the length of the curved part of the backup roll is denoted as ℓ_b (see Figure 2).

$$D_B(z) = 1400 + 2h_c \sqrt{1 - z/\ell_b} \quad (1)$$

$$D_W(z) = 660 - 2h_w \sqrt{1 - z/\ell_a} \quad (2)$$

Due to the contact with the work roll, the backup roll's deformation causes different deflections at $z = 0$ and $z = 900$ mm, which can be expressed as $\delta_{z=900} - \delta_{z=0} = 0.2$ mm. Also, the maximum wear appearing on the work roll can be estimated as $h_w = 0.3$ mm. By considering those profiles, the backup roll's crown is set as $h_c = 0.5$ mm ($= 0.2$ mm + 0.3 mm).

Table 2 shows the material properties of the rolls used in the analysis.^[46] High-chrome steel is used for the backup roll, HSS is used for the outer layer of the work roll, and DCI is used for the inner layer of the work roll. The outer layer HSS has a thickness of 60 mm ($r = 270\text{--}330$ mm).

Figure 3 shows stress–strain diagrams of both the HSS layer and the DCI layer of the work roll at room temperature. **Table 3** shows the chemical composition (mass, %) of both layers in the work roll.^[31] As shown in Table 3, the outer layer HSS contains about 2% carbon and the inner layer contains about 3% carbon. In the casting process, the outer layer HSS is casted first; then, after the outer layer's inner surface almost solidified, the inner layer DCI casting starts. During the DCI casting, the solidified inner surface of HSS is melted again causing the components of the outer layer HSS and inner layer DCI are mixed together around the HSS/DCI boundary. Due to this mixture, the carbides and graphite become unevenly distributed around the HSS/DCI boundary forming a fragile microstructures.

Table 1. Roll dimensions and loading condition (base value).

Size	Work roll	Backup roll	Rolled steel
Diameter [mm]	$D_W = 660$	$D_B = 1400$	–
Length/width [mm]	$L = 1800$	$L = 1800$	$W = 1200$
Rolling force, P_{total} [kN] ^{a)}	$P_{total} = 16400$		
Line force, p_B from backup roll [kN mm ⁻¹]	$p_B = P_{total}/L = 9.1$		
Line force, p_S from rolled steel [kN mm ⁻¹]	$p_S = P_{total}/W = 13.7$		

^{a)}Inlet thickness: 4.9 mm, outlet thickness: 3.3 mm, contact width: 23 mm

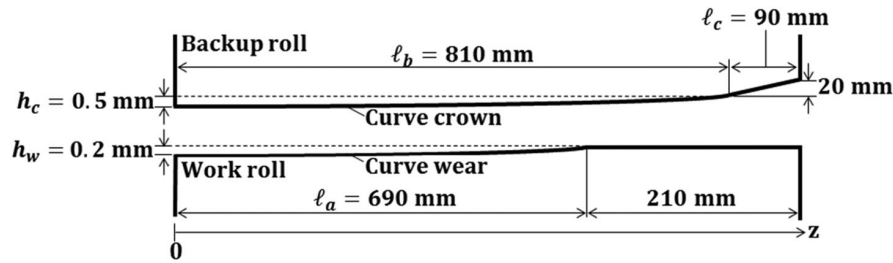


Figure 2. Backup roll's crown profile with $h_c = 0.5$ mm and work roll's wear profile with $h_w = 0.2$ mm.

Table 2. Material properties of the rolls.

Property	HSS	DCI	Backup roll
Tensile strength [MPa]	1575	415	1575
Fatigue strength ^[46] [MPa]	630	166	630
Yield strength [MPa]	1270	410	–
Young's modulus [GPa]	230	174	210
Poisson's ratio	0.3	0.28	0.3
Density [kg/m ³]	7600	7300	7800

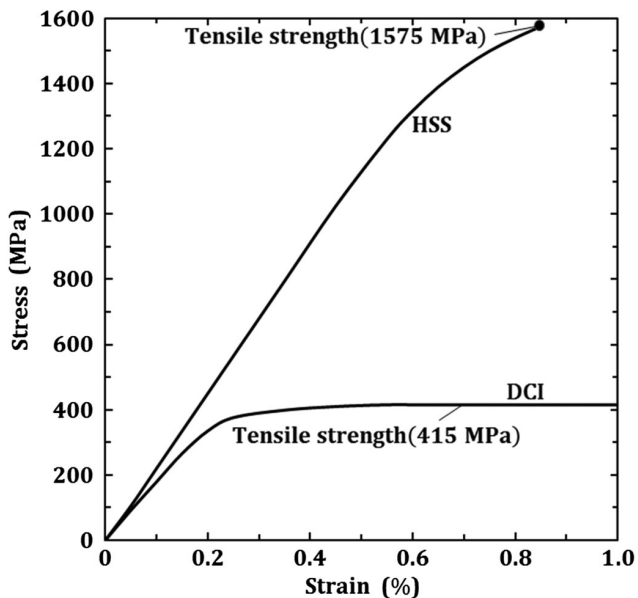


Figure 3. Stress–strain relation for HSS and DCI of the work roll.

Considering those situation, the risk of fatigue fracture around the HSS/DCI boundary will be focused in this study.

The software MSC Marc/Mentat 2012 is used to carry out the 3D elastic–plastic analysis. As it is not clear whether plastic

deformation occurs with respect to the internal stress of the work roll, elastic–plastic analysis was used in this analysis. **Figure 4** shows the FEM analysis model. The minimum mesh is $30 \times 30 \times 30$ mm³ and the element types used are four-contact tetrahedral element type and eight-contact hexahedral element type at the stress concentration part. The number of nodes is 23 883 and the number of elements is 21 410. The direct constrain method is used for contact analysis between work roll and backup roll. In this study, the previous residual stress analysis^[30–33] described in **Appendix A** is extended to rolling stress analysis. First, the same simulation is carried out using 3D modeling in **Figure 4** instead of the axisymmetric FEM modelling used in the previous study. After the residual stress is obtained, the consecutive rolling stress analysis described in Section 4 starts using the residual stress as an initial condition. The obtained results are reflecting both residual stress and rolling stress.

3. Residual Stress Generated in the Bimetallic Work Roll is used as an Initial Condition to the Rolling Stress Analysis

In this study, the roll residual stress is considered as an initial condition of the rolling stress analysis. As the detail of the residual stress simulation is described in the previous papers,^[30–33] the outline of residual stress simulation is briefly introduced in the Appendix A. In roll companies, the surface residual stress of the roll is always confirmed after tempering the roll using the nondestructive inspections such as X-ray diffraction method and ultrasonic method. The authors previous simulation has provided the residual stress distribution from the surface to the inside of the roll due to various different heat treatments. Previously, as the internal stress cannot be obtained using these nondestructive method, the destructive inspections such as Sachs boring method and disk cut method were sometimes applied spending high cost and time-consuming effort.^[47,48] The outline of the disk cut method with is indicated in **Appendix B** with the accuracy discussion in the previous paper.^[49]

Table 3. Chemical compositions of the work roll (mass, %).

Element	C	Si	Mn	P	S	Ni	Cr	Mo	Co	V	W	Mg
HSS	1–3	<2	<1.5	<1	<1	<5	2–7	<10	<10	3–10	<20	<10
DCI	2.5–4	1.5–3.1	<1	<.01	<.01	0.4–5	0.01–1.5	0.1–1	<1	<1	<1	0.02–0.08

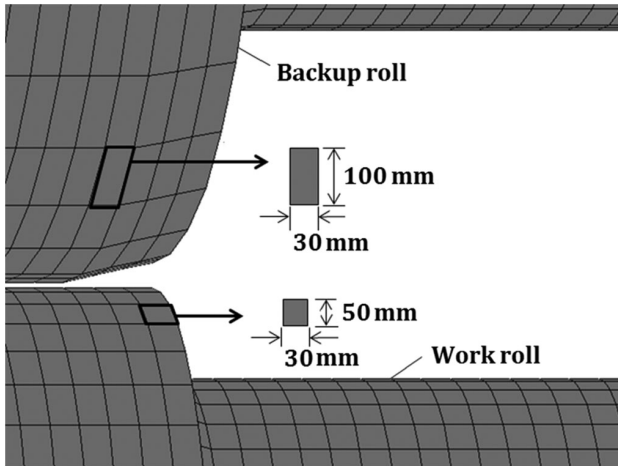


Figure 4. FEM mesh for backup roll and work roll.

Figure 5 shows the residual stresses σ_r , σ_θ , and σ_z after the preheating, quenching, and tempering treatment (see Appendix A). Figure 5a shows the residual stresses σ_r , σ_θ ,

and σ_z at fixed $z = 0$ when $0 \leq r \leq 330$ mm. In Figure 5a, the tensile stress σ_z is balanced with the compressive stress σ_z . Figure 5b shows the results at the boundary $r = 270$ mm along z -direction. The tensile stress σ_r which may cause debonding is almost constant along the z -direction. These residual stresses can be analyzed considering two tempering processes as described details in previous studies^[30–33] using the axisymmetric FEM model.

The previous residual stress analysis^[30–33] can be extended to rolling stress analysis in this article in the following way. First, the same simulation is carried out using 3D modelling instead of the axisymmetric FEM modeling used in the previous study. Then, after the residual stress is obtained, the consecutive rolling stress starts using the residual stress as an initial condition. The obtained results are reflecting both residual stress and rolling stress.

Figure 6 shows an example of the boundary failure considered in this article. As shown in Figure 6a, a semielliptical beach mark can be clearly seen near the grain graphite (Grain)/flaky graphite cast iron (FC) boundary at point A, which shows that the fatigue crack initiates at the inner boundary point A and propagates to the surface.^[20] Roll maker companies also identified that

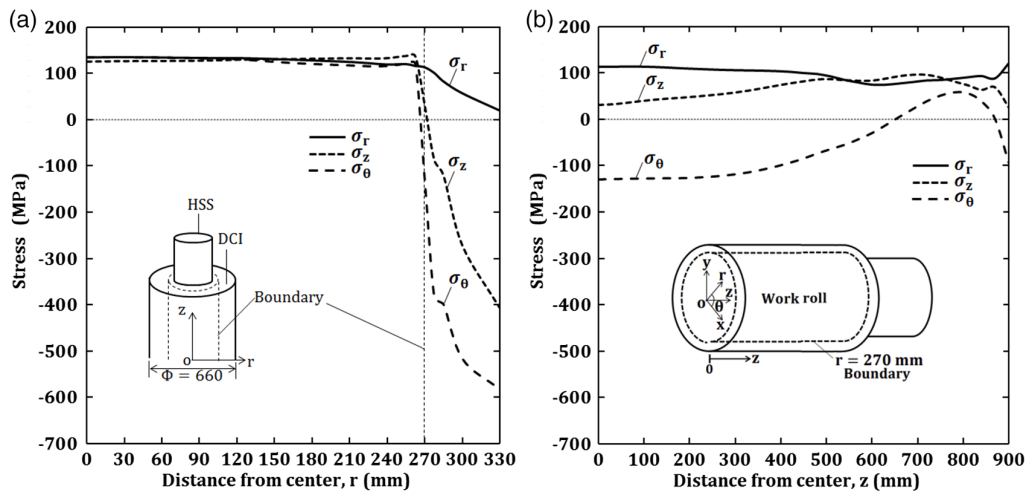


Figure 5. The generated residual stresses σ_r , σ_θ , and σ_z at the boundary $r = 270$ mm after the heating, quenching, and tempering treatment in a) radial direction at $z = 0$, and b) axial direction at the boundary $r = 270$ mm.

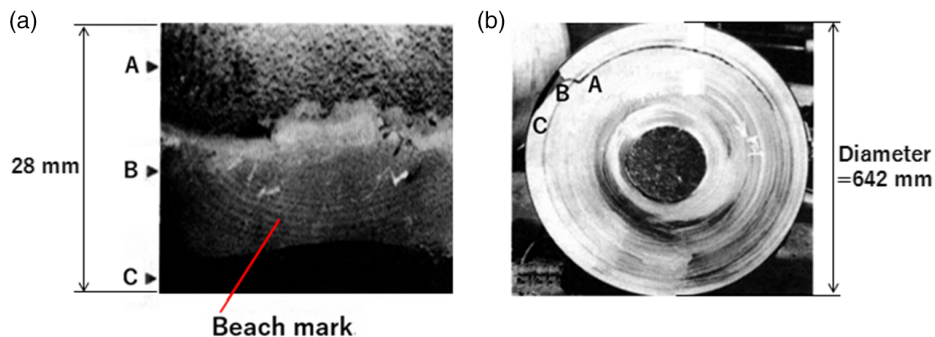


Figure 6. Boundary failure where the crack originated at grain/FC boundary in bimetallic work roll and propagates toward the surface. a) Fractured surface, A: Near boundary, B: Shell with beach mark, C: Roll surface, b) cross-sectional view of spalling crack Reproduced with permission.^[20] Copyright 1987, The Iron and Steel Institute of Japan.

sometimes similar failure can be seen near the end of the roll body (see point B_{750}^{270} in Figure 9). Such peeling shown in Figure 6 is caused by the radial stress σ_r variation during the roll rotation. In this article, this internal fatigue failure caused by σ_r will be studied as the previous papers only focused on the surface spalling in backup rolls.^[21–29] This surface failure starts from several mm inside from the surface caused by the shear stress under rolling fatigue is very different from the failures in Figure 6 caused by σ_r in Figure 5.

4. Rolling Stress Generated in the Bimetallic Work Roll Obtained by the Consecutive FEM Analysis

In this section, the rolling stress is discussed when the bimetallic work roll with the residual stress in Section 3 is used in the four-high rolling mill, as shown in Figure 1. Considering the boundary debonding previously reported as well as the roll center fracture, the risk of fatigue failure is evaluated at those critical points. In this evaluation, the repeated maximum and minimum values of σ_r appearing at each roll rotation should be considered as the driving force causing the internal fatigue failure.^[50]

To estimate the maximum stress amplitude σ_r controlling the internal fatigue failure, Figure 7 shows the several critical lines denoted by $B_{0-900}^{270}|\theta=-90^\circ$, $B_{0-900}^{270}|\theta=90^\circ$, $B_{0-900}^{270}|\theta=0^\circ$, $C_{0-900}^0|\theta=90^\circ$, and $C_{0-900}^0|\theta=0^\circ$ assumed inside of the work roll. For example, $B_{0-900}^{270}|\theta=-90^\circ$ denotes the line at $r = 270$ mm, $\theta = -90^\circ$, $z = 0-900$ mm. The superscript 270 of $B_{0-900}^{270}|\theta=-90^\circ$ represents the r -coordinate $r = 270$ mm, and the subscript 0–900 of $B_{0-900}^{270}|\theta=-90^\circ$ represents the z -coordinate $z = 0-900$ mm. As shown in Table 1, p_B denotes the line force applied to the work roll from the backup roll, and p_S denotes the line force applied to the work roll from the rolled steel.

To estimate the rolling stress variation due to the contact of the rolled steel from $\theta = -90^\circ$, Figure 8 shows the stress distributions σ_r along the z -direction denoted by $B_{0-900}^{270}|\theta=-90^\circ$ and $B_{0-900}^{270}|\theta=0^\circ$ on the boundary $r = 270$ mm. Note that, the stress variation is largest between the angle $-90^\circ \leq \theta \leq 0^\circ$. This is because the maximum tensile stress σ_r appears at $\theta = 0^\circ$ and the

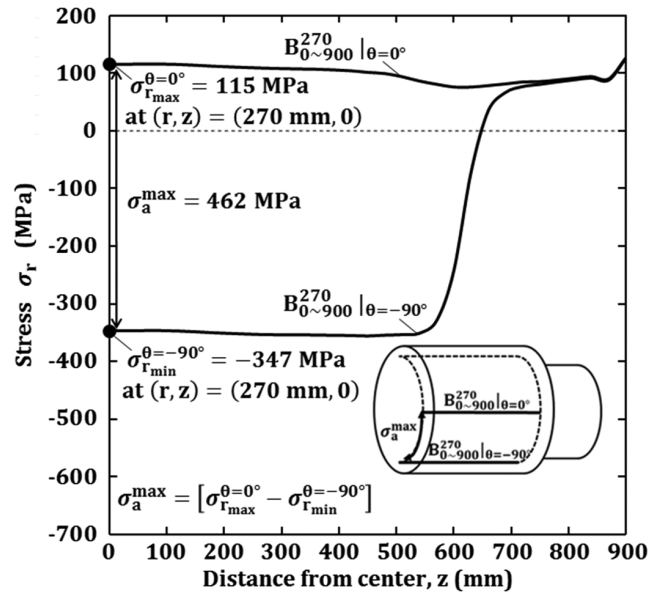


Figure 8. Variation of the stress distribution σ_r at the boundary $r = 270$ mm due to the contact of the rolled steel from $\theta = -90^\circ$.

maximum compressive stress σ_r appears at $\theta = -90^\circ$. As σ_r in Figure 5b is almost equal to σ_r in Figure 8, the rolling stress $\sigma_r \cong 0$ at $\theta = 0^\circ$. Figure 8 also shows the largest compressive stress appears in the range of $0 \leq z < 600$ mm because the rolled steel width is 600 mm. In Figure 8, the stress amplitude is considered in the region $0 \leq z \leq 600$ mm. Then, it is found that the maximum stress amplitude appears at $(r, z) = (270 \text{ mm}, 0)$ where the maximum tensile stress $\sigma_{r \max}^{\theta=0^\circ} = 115$ MPa, the maximum compressive stress $\sigma_{r \min}^{\theta=-90^\circ} = -347$ MPa, and maximum stress amplitude $\sigma_a^{\max} = \sigma_{r \max}^{\theta=0^\circ} - \sigma_{r \min}^{\theta=-90^\circ} = 462$ MPa. This maximum stress amplitude at $(r, z) = (270 \text{ mm}, 0)$ is denoted by $B_{0-900}^{270}|\text{Rolled steel}$ to discuss the fatigue failure.

To estimate the rolling stress variation due to the contact of the backup roll from $\theta = 90^\circ$, Figure 9 shows the stress distributions σ_r denoted by $B_{0-900}^{270}|\theta=90^\circ$ and $B_{0-900}^{270}|\theta=0^\circ$ along the z -direction on the boundary $r = 270$ mm. The stress variation is largest between

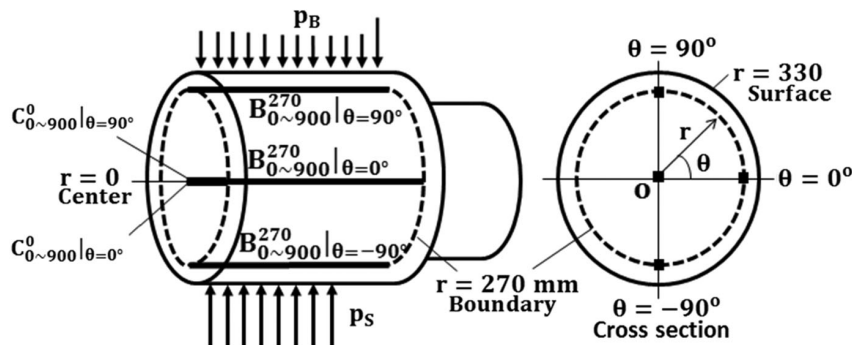


Figure 7. Illustration of the critical lines $B_{0-900}^{270}|\theta=-90^\circ$, $B_{0-900}^{270}|\theta=90^\circ$, $B_{0-900}^{270}|\theta=0^\circ$, $C_{0-900}^0|\theta=90^\circ$, and $C_{0-900}^0|\theta=0^\circ$ where σ_r distributions are considered. The three lines $B_{0-900}^{270}|\theta=-90^\circ$, $B_{0-900}^{270}|\theta=90^\circ$, and $B_{0-900}^{270}|\theta=0^\circ$ are on the boundary $r = 270$ mm. Two lines along the roll center $r = 0$ $C_{0-900}^0|\theta=90^\circ$, and $C_{0-900}^0|\theta=0^\circ$ denote that σ_r distributions are considered in the $\theta = 0^\circ$ and $\theta = 90^\circ$ directions.

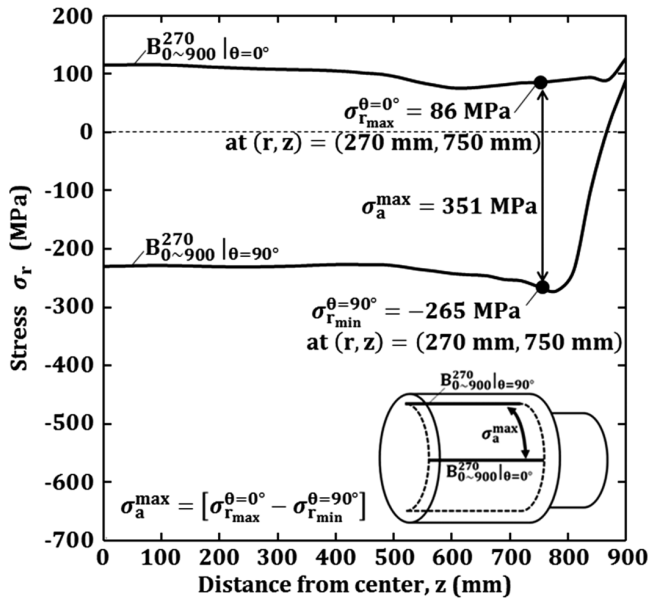


Figure 9. Variation of the stress distribution σ_r at the boundary $r = 270$ mm due to the contact of the backup roll from $\theta = 90^\circ$.

the angle $0^\circ \leq \theta \leq 90^\circ$. In Figure 9, the stress amplitude is considered in the region $0 \leq z \leq 810$ mm. Then, it is found that the maximum stress amplitude appears at $(r, z) = (270, 750)$ mm from the tensile stress $\sigma_{r_{\max}}^{\theta=0^\circ} = 86$ MPa and the compressive stress $\sigma_{r_{\min}}^{\theta=90^\circ} = -265$ MPa. The maximum stress amplitude $\sigma_a^{\max} = \sigma_{r_{\max}}^{\theta=0^\circ} - \sigma_{r_{\min}}^{\theta=90^\circ} = 351$ MPa at $(r, z) = (270, 750)$ mm is denoted by $B_{750}^{270}|_{\text{Backup roll}}$ to discuss the fatigue failure.

Next, to evaluate the risk of the roll center fracture, Figure 10 shows the stress distributions denoted by $C_{0-900}^0|_{\theta=90^\circ}$ and

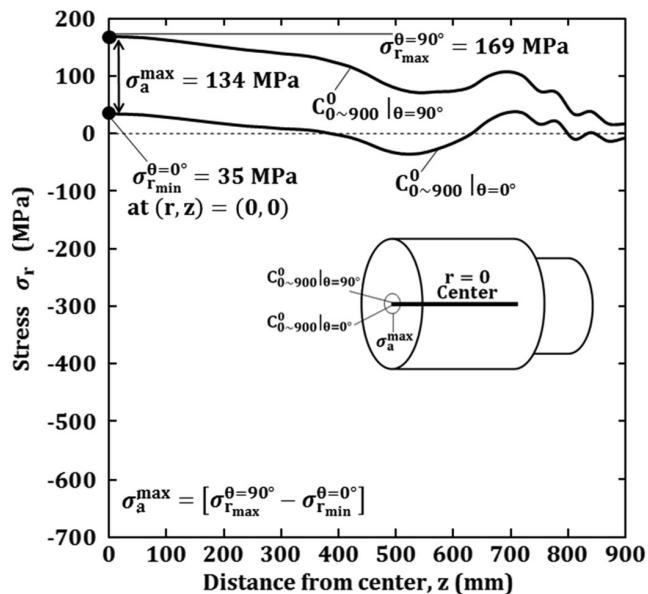


Figure 10. Variation of the stress distribution σ_r at the roll center at $r = 0$ mm due to the contact of the rolled steel and the backup roll.

$C_{0-900}^0|_{\theta=0^\circ}$ at the roll center at $r = 0$. The maximum stress amplitude σ_r can be seen at $z = 0$ from the maximum tensile stress is $\sigma_{r_{\max}}^{\theta=90^\circ} = 169$ MPa and the minimum tensile stress $\sigma_{r_{\min}}^{\theta=0^\circ} = 35$ MPa. The maximum stress amplitude $\sigma_a^{\max} = \sigma_{r_{\max}}^{\theta=90^\circ} - \sigma_{r_{\min}}^{\theta=0^\circ} = 134$ MPa at $(r, z) = (0, 0)$ is denoted by C_0^0 to discuss the fatigue failure.

5. Fatigue Risk Evaluation for Three Critical Points

Figure 11 shows three critical points $B_0^{270}|_{\text{Rolled steel}}$, $B_{750}^{270}|_{\text{Backup roll}}$, and C_0^0 , as shown in Figure 8, 9, and 10. Table 4 shows the maximum stress, the minimum stress, the mean stress, and the stress amplitude at those three critical points during the roll rotation. Among them, $B_0^{270}|_{\text{Rolled steel}}$ and $B_{750}^{270}|_{\text{Backup roll}}$ are subjected to quite large alternative compressive stress. Fatigue failure under large compressive stress was treated by several previous papers focusing on ball/roller bearings and backup roll surfaces.^[51,52] They studied rolling contact fatigue only without considering fatigue in general. In other words, no data is available for ordinary fatigue strength under large compressive stress fields.^[53] Considering this situation, the endurance limit lines are newly prescribed under large compressive stress as no studies can be seen.

Several fatigue experimental studies investigated the fatigue life under the compressive mean stress.^[54-56] Figure 12 shows three types of compressive alternative loading where the mean stress < 0 . The fatigue life consists of a crack initiation period, crack growth period, and finally ultimate failure. During the crack initiation stage, the fatigue life is controlled by the stress amplitude irrespective of the mean stress, positive or negative. Under the fixed stress amplitude, as shown in Figure 12, the

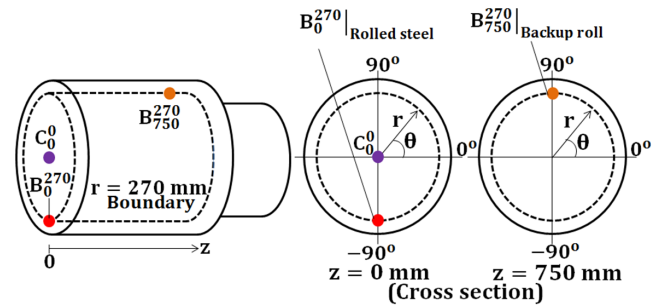


Figure 11. Illustration of three critical points denoted by $B_0^{270}|_{\text{Rolled steel}}$, $B_{750}^{270}|_{\text{Backup roll}}$, and C_0^0 where fatigue risk should be evaluated based on the analysis and experience.

Table 4. Maximum stress, minimum stress, mean stress, and stress amplitude at three critical points.

Point	$\sigma_{r_{\max}}$	$\sigma_{r_{\min}}$	σ_m	σ_a
$B_0^{270} _{\text{Rolled steel}}$	115	-347	-116	231
$B_{750}^{270} _{\text{Backup roll}}$	86	-265	-90	176
C_0^0	169	35	102	67

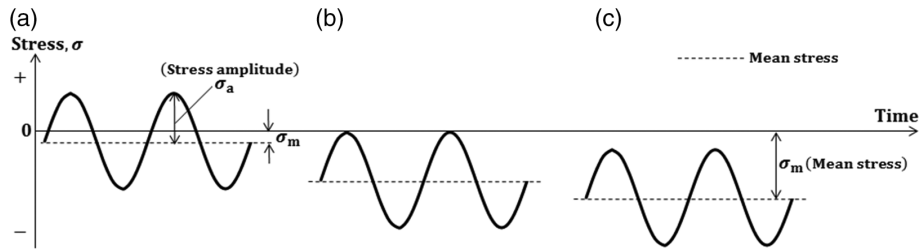


Figure 12. Three types of compressive alternative loading where the mean stress $\sigma_m < 0$. a) $\sigma_a + \sigma_m = \sigma_{\max} > 0$; b) $\sigma_a + \sigma_m = \sigma_{\max} = 0$; c) $\sigma_a + \sigma_m = \sigma_{\max} < 0$.

crack initiates at the same time.^[54] Instead, during the crack growth stage, with decreasing the mean stress, the crack growth rate decreases sensitively and the fatigue life increases significantly. It is known that under $\sigma_{\max} = 0$ in Figure 12b and $\sigma_{\max} < 0$ in Figure 12c, the crack does not propagate and no final failure.^[54,55] However, under $\sigma_{\max} > 0$ in Figure 13a, the amount of tensile stress $\sigma_{\max} = \sigma_a + \sigma_m > 0$ necessary for the final failure is unknown because it has not been discussed yet until now. It varies depending on the magnitude of $\sigma_m < 0$.

Figure 13 shows a stress amplitude versus mean stress diagram (σ_a - σ_m diagram) to discuss the fatigue limit under large compressive alternative loading $\sigma_m \leq 0$. First of all, assume the amount of the ultimate tensile strength σ_B can be applied to the compressive stress $\sigma_m < 0$ and alternative stress $\sigma_a > 0$. They can be expressed in Equation (3).

$$|\sigma_m| < \sigma_B, |\sigma_a| < \sigma_B \quad (3)$$

Assume the so-called modified Goodman law defined in Equation (4) for $\sigma_m \geq 0$.

$$\frac{\sigma_a}{\sigma_{w0}} + \frac{\sigma_m}{\sigma_B} \leq 1 \quad (4)$$

The limit line $\sigma_a/\sigma_{w0} + \sigma_m/\sigma_B = 1$ can be extended to the negative region $\sigma_m < 0$.^[57]

Consider pulsating compressive loading $\sigma_a + \sigma_m = \sigma_{\max} = 0$ in Figure 12b. In Figure 13, the line is indicated as $\sigma_m = -\sigma_a$ denoted by a dotted line with the angle of 45° from the ordinate from the origin. As described earlier, no fatigue final failure happens in the region (5).

$$\sigma_a + \sigma_m = \sigma_{\max} \leq 0 \quad (5)$$

Denote the intersection $\sigma_a/\sigma_{w0} + \sigma_m/\sigma_B = 1$ and $\sigma_a + \sigma_m = 0$ as point E (see Figure 13c). As point E satisfies Equation (5), there is no final fracture. Therefore, instead of point E, point F should be considered as the fatigue limit by applying a certain amount of positive tensile stress to cause final failure.^[58] Consider fully reversible fatigue limit at point D (see Figure 13b) where the maximum tensile/compressive stress $\sigma_r = 166$ MPa is applied. At point E, the maximum compressive stress

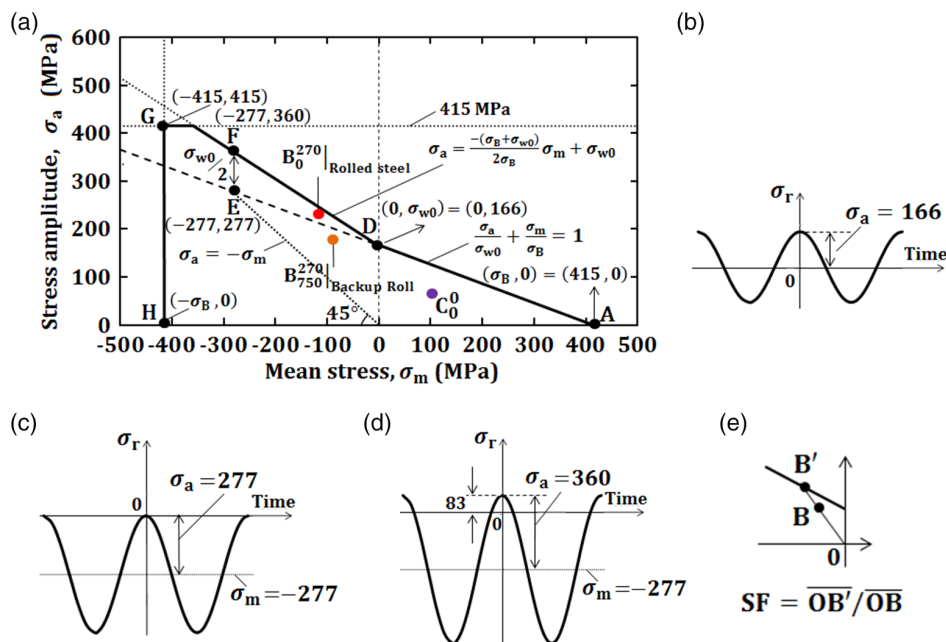


Figure 13. a) Stress amplitude versus mean stress diagram to evaluate the fatigue failure at three critical points; b) Stress at point D; c) Stress at point E; d) Stress at point F; and e) Safety factor definition.

$\sigma_r = 554 \text{ MPa} = 277 \text{ MPa} \times 2$ is more than three times larger than the one of point D and more severe damage is accumulated. Then, the amount of the tensile stress necessary for point F should be smaller than that at point D. Assume half value $\sigma_{w0}/2 = 83 \text{ MPa}$ is necessary for this tensile stress at point F (see Figure 13d). By drawing the line through point D and point F in Figure 13, the fatigue limit can be estimated. The range can be expressed by the following equation.

$$\sigma_a \leq -\frac{\sigma_B + \sigma_{w0}}{2\sigma_B} \sigma_m + \sigma_{w0} \quad (6)$$

For large compressive alternative loading, the fatigue limit is determined from Equation (3)–(6), which is expressed by the thick solid lines passing through points A, D, F, G, H in Figure 13a. Figure 13a shows the three critical points' results $B_0^{270}|_{\text{Rolled steel}}$, $B_{750}^{270}|_{\text{Backup roll}}$, and C_0^0 in Table 4.

Table 5 shows the safety factor defined as $SF = \overline{OB'}/\overline{OB}$ in Figure 13e. A larger SF value means the point is relatively safer than another point having a smaller SF value. Therefore, the safety factor SF can be used to evaluate the risk of fatigue failure relatively. Although the safety factor $SF \geq 1$, $B_0^{270}|_{\text{Rolled steel}}$ is relatively more dangerous than $B_{750}^{270}|_{\text{Backup roll}}$ and C_0^0 . The results showed that the fatigue crack initiation around points B_0^{270} on the HSS/DCI boundary may contribute to several roll failures previously occurred.

Although C_0^0 is relatively safer, material defects often observed at the roll center are not considered in Figure 13a. Hidaka et al. evaluated the maximum defect size by using statistics of extremes in the DCI specimens and confirmed that the lowest fatigue limit of DCI joints is larger than welded joints.^[59,60] To evaluate the fatigue failure risk at the roll center point C_0^0 more accurately, in this study, the following formula is applied.^[61]

$$\sigma_{w0} = \frac{1.56(H_V + 120)}{(\sqrt{\text{area}})^{1/6}} \quad (7)$$

Here, σ_{w0} is in MPa and is the fatigue limit under fully reversed loading of a material containing a defect; H_V is in kgf mm^{-2} and is the Vickers hardness number; and $\sqrt{\text{area}}$ is in μm and is the square root of defect/crack area projected normal to the maximum principal stress. Figure 14 shows the fatigue limit σ_{w0} when the spheroidal defect diameter $2a = 0, 5000, 10000 \mu\text{m}$ is assumed through $\sqrt{\text{area}} = \sqrt{\pi a^2}$. Here, the defect size $5 \text{ mm} (= 5000 \mu\text{m})$ is empirically known for the roll maker companies, and for the safety reason, $10 \text{ mm} (= 10000 \mu\text{m})$ defect size is also considered. Figure 14 shows that the fatigue limit σ_{w0} decreases from

Table 5. Safety factor defined as $SF = \overline{OB'}/\overline{OB}$ in Figure 13e for three critical points by applying the consecutive FEM analysis.

Point	Safety factor, SF
$B_0^{270} _{\text{Rolled steel}}$	1.09
$B_{750}^{270} _{\text{Backup roll}}$	1.43
C_0^0	1.55

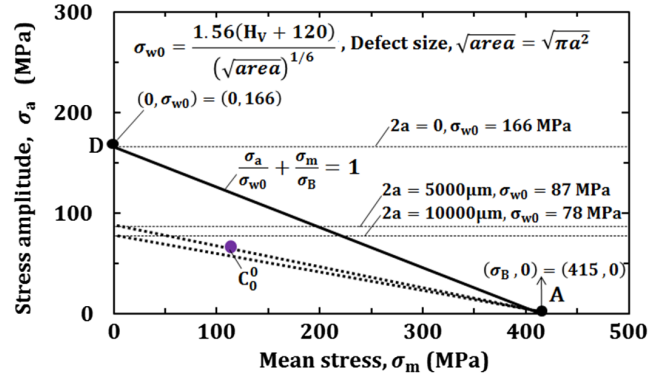


Figure 14. Stress amplitude versus mean stress diagram to evaluate the fatigue failure at point C_0^0 when the spheroidal defect diameter $2a = 0, 5000, 10000 \mu\text{m}$ is assumed through $\sqrt{\text{area}} = \sqrt{\pi a^2}$.

Table 6. Safety factor $SF = \overline{OB'}/\overline{OB}$ defined as $SF = \overline{OB'}/\overline{OB}$ in Figure 14 for the critical point C_0^0 when the spheroidal defect diameter $2a = 0, 5000, 10000 \mu\text{m}$ is assumed through $\sqrt{\text{area}} = \sqrt{\pi a^2}$.

Diameter change [μm]	Safety factor, SF
$2a = 0$	1.55
$2a = 5000$	0.98
$2a = 10000$	0.91

$\sigma_{w0} = 166 \text{ MPa}$ to $\sigma_{w0} = 87 \text{ MPa}$ when the defect diameter is changed from $2a = 0$ to $2a = 5000 \mu\text{m}$. When $2a = 10000 \mu\text{m}$, the fatigue limit σ_{w0} decreases to $\sigma_{w0} = 78 \text{ MPa}$. Table 6 shows that the safety factor SF decreases with increasing the defect size. Figure 14 shows that the point C_0^0 becomes dangerous depending on the defect dimensions. If the defect size is 5 mm , the risk of fatigue failure at the point C_0^0 is larger than the point C_0^0 without defect in Table 5.

6. Rolling Stress Estimation by Superposing the Residual Stress and the Rolling Stress

As shown in Figure 15a, in this study, the consecutive analysis is carried out from the residual stress to the rolling stress to evaluate the fatigue failure risk. Then, the critical points $B_0^{270}|_{\text{Rolled steel}}$, $B_{750}^{270}|_{\text{Backup roll}}$, and C_0^0 are considered on the σ_a - σ_m diagram. However, in the real roll rotation, the results of σ_a and σ_m may change because the plastic stress varies depending on the loading history. As another consecutive analysis has to be done every roll rotation, lots of calculation is necessary to clarify the differences. Therefore, in this section, a simple evaluation method is considered. Figure 15b shows the method of superposition, which simply superposes the residual stress and the rolling stress.

Figure 16 shows the stress amplitude versus mean stress diagram for the three critical points obtained by simply superposing the residual stress and the rolling stress, as shown in Figure 15b.

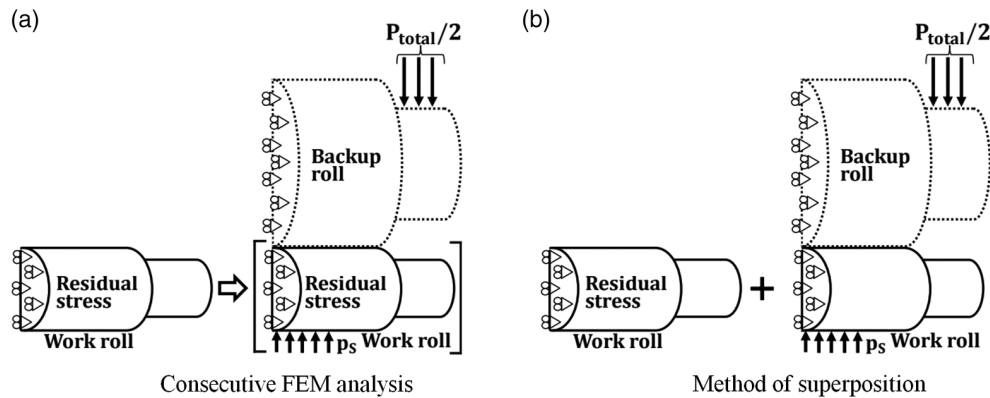


Figure 15. Comparison between two different methods of the rolling stress.

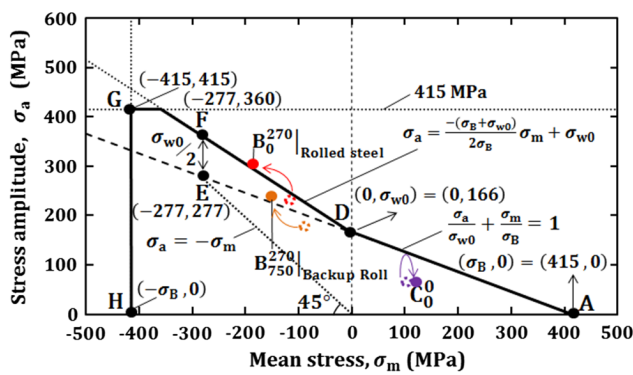


Figure 16. Stress amplitude versus mean stress diagram to evaluate the fatigue failure at three critical points denoted by the colored solid circles obtained by superposing the residual stress and the rolling stress in comparison with the dotted circle obtained by the consecutive FEM.

Table 7. Comparison of safety factor obtained by consecutive FEM (dotted circles in Figure 16) and simple superposition (solid circles in Figure 16) regarding three critical points.

Point	By consecutive FEM analysis	By superposition
B_0^{270} Rolled steel	1.09	> 0.95
B_{750}^{270} Backup roll	1.43	> 1.27
C_0	1.55	> 1.49

Table 7 compares the safety factor SF obtained by the superposition with the results of the previous consecutive FEM analysis. As shown in Table 7, the SF of the superposition is smaller than the SF of the consecutive analysis. In other words, the superposition method may evaluate the risk of failure in a safer way because the FEM consecutive results in Figure 15a are safer than the results of the superposition in Figure 15b. It may be concluded that we can estimate the rolling stress by simply superposing the results. The results in Table 7 can be compared for the loading history of different entire rolling campaign for typical strip steel grade.

7. Conclusions

In this study, the 3D elastic–plastic contact FEM is applied to calculate the rolling stress generated in bimetallic work roll during rolling in a four-high rolling mill. The initial residual stress was considered and the consecutive analysis was carried out to evaluate the risk of fatigue failure. This study assumed the following rolling conditions that can be regarded as the average values in present steelworks,^[34] where the work roll diameter $D_W = 660$ mm with the length $L = 1800$ mm, the high chrome steel backup roll diameter of $D_B = 1400$ mm with the length $L = 1800$ mm, the width of the rolled steel $W = 1200$ mm and the standard rolling force $P_{total} = 16400$ kN.^[34,35] The conclusions obtained can be summarized in the following way. 1) The consecutive FEM analysis for quenching–tempering–rolling was performed to evaluate the risk of fatigue failure. By focusing on three critical points based on the analysis and experience, it may be concluded that the most critical point is located at the HSS/DCI boundary point B_0^{270} where $(r, z) = (270, 0)$ because of the rolling steel caused the largest amplitude. Another critical point is also located at B_{750}^{270} where $(r, z) = (270, 750)$ mm because of the backup roll contact. 2) Using the relative safety factor SF, the fatigue failure risk was discussed. The results showed that the fatigue crack initiation around points B_0^{270} and B_{750}^{270} on the HSS/DCI boundary may contribute to several roll failures previously occurred. 3) As the consecutive FEM analysis considering each roll rotation is time consuming, the simple evaluation method was discussed by superposing the residual stress and the rolling stress. The results showed that the superposition method may evaluate the risk of failure in a safer way because the FEM consecutive results in Figure 16a are safer than the results of the superposition in Figure 16b.

Appendix A. Outline of Residual Stress Simulation of the Bimetallic Work Roll

In this article, as shown in Figure 5, the residual stress distributions are obtained using the simulation method in the

previous paper.^[30–33] In this Appendix A, the outline of residual stress simulation is briefly introduced. Along with intensifying international competition in the steel industry, the high quality of rolled products is becoming more stable under more severe rolling conditions. As the residual stress in work roll is closely related to those technical issues and manufacturing costs, roll companies applied many practical measuring methods including X-ray diffraction method and ultrasonic method to confirm the roll surface residual stress. As the internal stress cannot be obtained using these nondestructive methods, the destructive inspections such as Sachs boring method and disk cut method are sometimes applied spending high cost and time-consuming effort.^[47,48] In this sense, the residual stress simulation has been requested to obtain the residual stress distribution from the surface to the inside of the roll under various different heat treatments.

Figure A1 shows the surface temperature history of the bimetallic work roll during heat treatment consisting of the preheating, quenching, and tempering. In preheating process, the whole roll is heated up to the uniform temperature of $T_{\text{Start}} = 1050^\circ\text{C}$ and kept for several hours. Then, the roll temperature drops rapidly through air cooling. After that, the roll is put into the furnace again and maintained at $T_{\text{Q,Keep}}$ to prevent excessive thermal stresses caused by rapid cooling. After keeping period, the roll is cooled down slowly until to the temperature of $T_{\text{T,Finish}}$. After the quenching process, the tempering process is carried out 2 times to release the residual stress and obtained the stable microstructure. After this process, the generated residual stress is used as an initial condition for the consecutive FEM analysis of the rolling analysis.

Predicting the residual stress of the bimetallic roll during preheating, quenching, and tempering, as shown in Figure 5, can be realized by FEM simulation efficiently with lower cost and higher accuracy compared with experimental measurement. In the previous studies,^[30–33] axisymmetric FEM model of a half-length of the roll was considered, as shown in Figure A2.

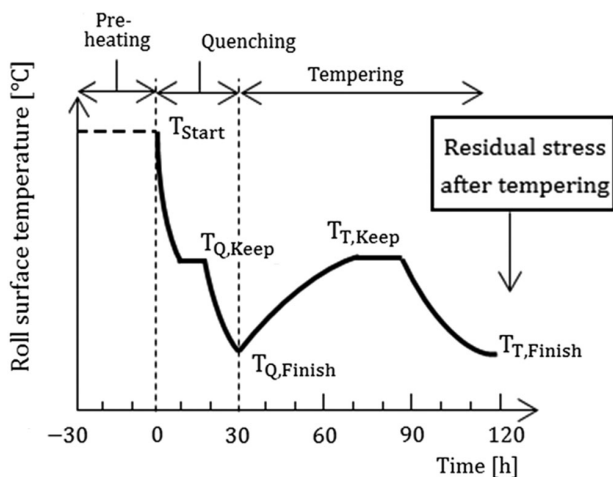


Figure A1. Heating, quenching, and tempering treatment of the bimetallic work roll.

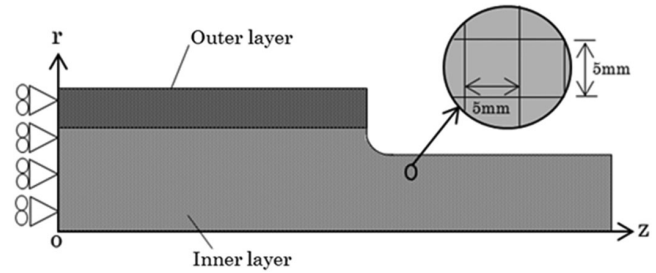


Figure A2. Axisymmetric FEM model of the bimetallic work roll to simulate the heating treatment.

Figure A3 shows the Young's modulus, thermal expansion coefficient, Poisson's ratio, stress–strain characteristic for both DCI and HSS, thermal conductivity, and specific heat during the quenching process. Figure A4 shows the stress distribution after quenching, after first tempering, and after second tempering. After the first tempering, the maximum tensile stress decreased by 35% and after the second tempering the maximum tensile stress decreased by 54%.

Appendix B. Outline of Disk Cut Method to Measure the Inside Residual Stress Inside of the Roll

In this Appendix B, the disk cut method is briefly introduced. Figure B1 shows a thin disk sliced from the roll cylinder around the middle portion.^[49] During the disk-slicing process, circumferential and axial strains at the cylinder surface were recorded with the aid of strain gauges. Since the axial stress σ_z^{Disk} on the sliced disk is completely released, the remaining residual stresses in the sliced disk are in plane stress. Then, the sliced disk stresses σ_r^{Disk} and $\sigma_\theta^{\text{Disk}}$ will be obtained to estimate the cylinder stress $\sigma_r^{\text{Cylinder}}$.

To calculate thermoelastic stresses of the cylinder and disk, the following equations are available. When a disk is subjected to the temperature distribution $T(r)$, the thermal stresses σ_r^{Disk} and $\sigma_\theta^{\text{Disk}}$ are given by Equation (B1), (B2). In contrast, the cylinder stresses $\sigma_z^{\text{Cylinder}}$, $\sigma_r^{\text{Cylinder}}$, and $\sigma_\theta^{\text{Cylinder}}$ are given by Equation (B3), (B4), and (B5).

$$\sigma_r^{\text{Disk}} = \alpha E \left(\frac{1}{b^2} \int_0^b T(r) r dr - \frac{1}{r^2} \int_0^r T(r) r dr \right) \quad (\text{B1})$$

$$\sigma_\theta^{\text{Disk}} = \alpha E \left(-T(r) + \frac{1}{b^2} \int_0^b T(r) r dr + \frac{1}{r^2} \int_0^r T(r) r dr \right) \quad (\text{B2})$$

$$\sigma_r^{\text{Cylinder}} = \frac{\alpha E}{1 - \nu} \left(\frac{1}{b^2} \int_0^b T(r) r dr - \frac{1}{r^2} \int_0^r T(r) r dr \right) = \frac{1}{1 - \nu} \sigma_r^{\text{Disk}} \quad (\text{B3})$$

$$\begin{aligned} \sigma_\theta^{\text{Cylinder}} &= \frac{\alpha E}{1 - \nu} \left(\frac{1}{b^2} \int_0^b T(r) r dr + \frac{1}{r^2} \int_0^r T(r) r dr - T(r) \right) \\ &= \frac{1}{1 - \nu} \sigma_\theta^{\text{Disk}} \end{aligned} \quad (\text{B4})$$

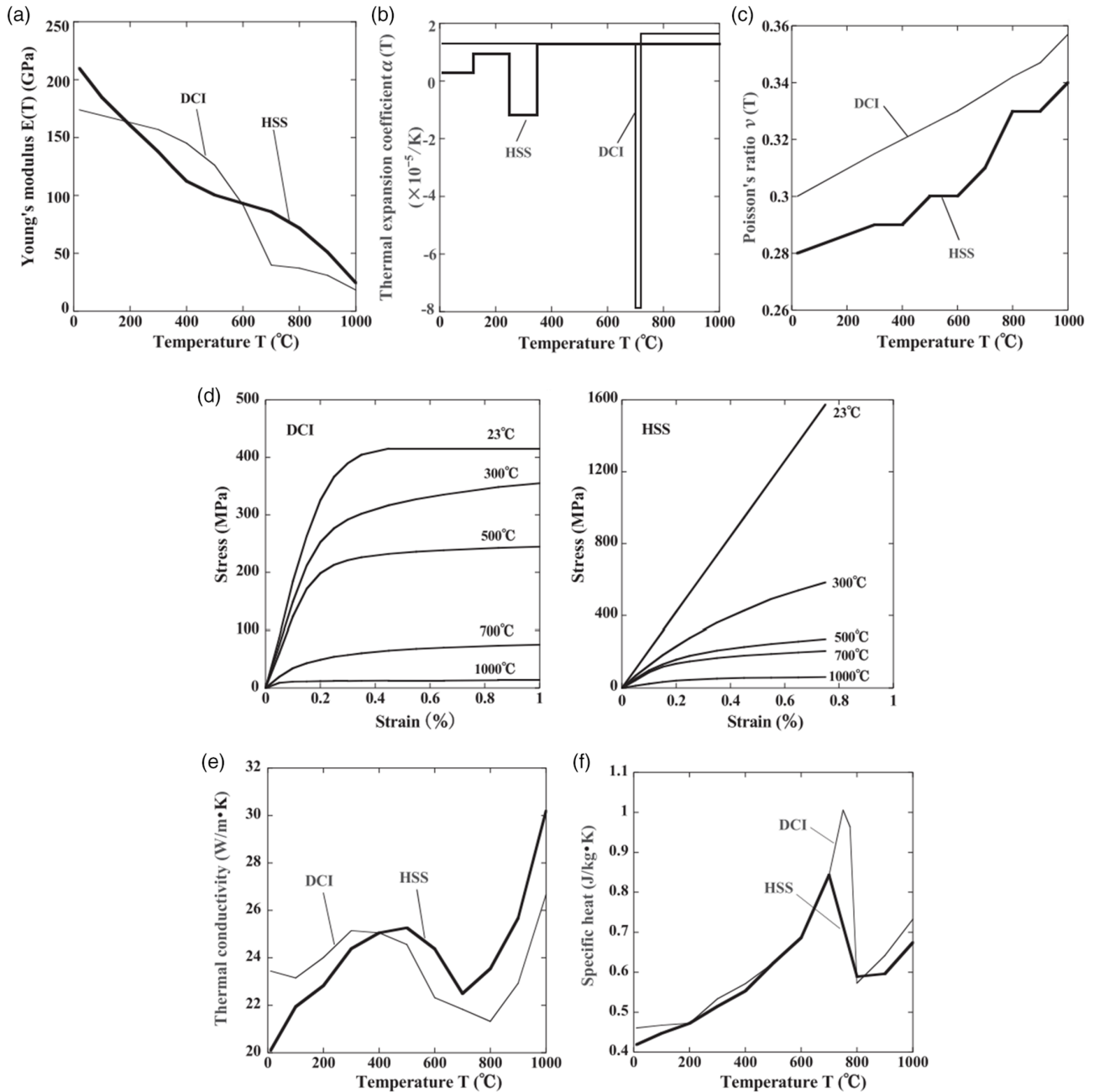


Figure A3. a) Young's modulus; b) thermal expansion coefficient; c) Poisson's ratio; d) stress-strain for DCI and HSS; e) thermal conductivity; and f) specific heat.

$$\sigma_z^{\text{Cylinder}} = \frac{\alpha E}{1 - \nu} \left(\frac{2}{b^2} \int_0^b T(r) r dr - T(r) \right) = \sigma_\theta^{\text{Cylinder}} + \sigma_r^{\text{Cylinder}} \quad (\text{B5})$$

From the aforementioned equations, the following relation between the disk stress and the cylinder stress under the same temperature distribution can be expressed as

$$\sigma_z^{\text{Cylinder}} = \frac{1}{1 - \nu} (\sigma_\theta^{\text{Disk}} + \sigma_r^{\text{Disk}}) \quad (\text{B6})$$

where b is the cylinder radius, $T(r)$ is the temperature distribution, E is the Young's modulus, α is the thermal expansion coefficient, and ν is the Poisson's ratio. As shown in Equation (B6), the stress $\sigma_z^{\text{Cylinder}}$ can be obtained exactly from the disk stress $\sigma_\theta^{\text{Disk}}$ and σ_r^{Disk} if there is no plasticity.

Figure B2 shows the stress ratio $\sigma_z^{\text{Cylinder}} / [(\sigma_r^{\text{Disk}} + \sigma_\theta^{\text{Disk}}) / (1 - \nu)]$ of the bimetallic roll under different quenching time using the same material properties in Appendix A.^[30–33]

Different from the elastic stress expressed by Equation (B6), the ratio varies depending on the quenching time. Care should

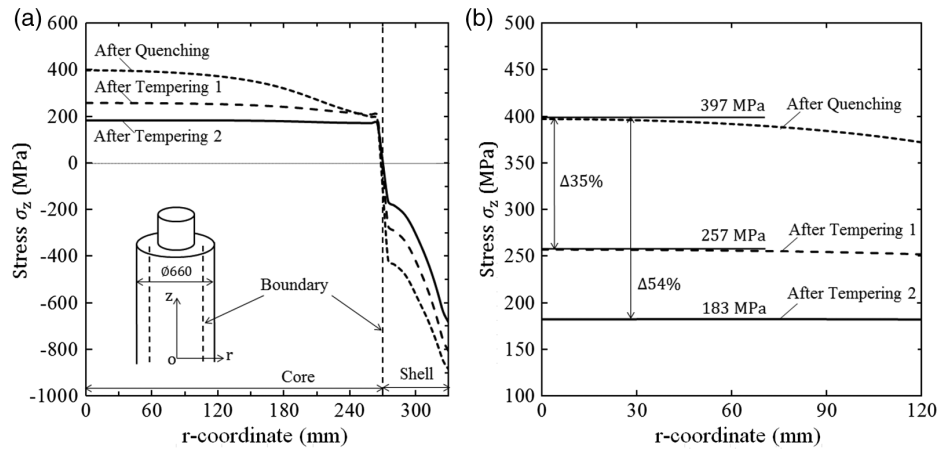


Figure A4. a) Stress distribution after quenching, after first tempering, and after second tempering. b) Details of maximum stress range.

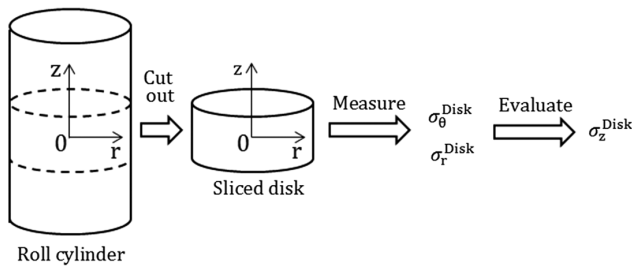


Figure B1. Schematic illustration how to obtain the internal stress of the roll using the disk cut method.

been expected to obtain the internal stress, it was proposed in the previous papers and indicated in Appendix A.

Conflict of Interest

The authors declare no conflict of interest.

Data Availability Statement

The data that support the findings of this study are available on request from the corresponding author. The data are not publicly available due to privacy or ethical restrictions.

Keywords

bimetallic work roll, fatigue failure, rolling mill, stress analysis

Received: May 26, 2021
Revised: September 4, 2021
Published online: October 27, 2021

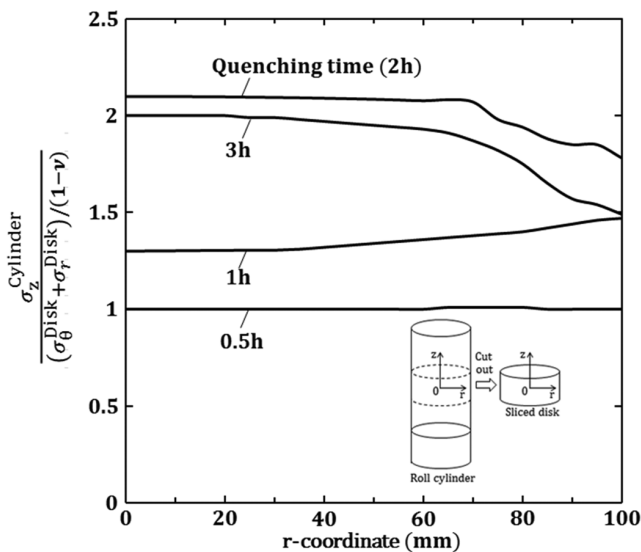


Figure B2. Stress ratio $\frac{\sigma_z^{\text{Cylinder}}}{[(\sigma_r^{\text{Disk}} + \sigma_\theta^{\text{Disk}})/(1 - \nu)]}$ near the roll center of the bimetallic roll under the different quenching time.

be taken for the ratio, which is larger than 1 for the most cases. Sometimes the value $\sigma_z^{\text{Cylinder}}$ is two times larger than the value $(\sigma_r^{\text{Disk}} + \sigma_\theta^{\text{Disk}})/(1 - \nu)$. As the numerical simulation method has

- [1] H. Shimoda, S. Onodera, K. Hori, *Trans. Jpn. Soc. Mech. Eng.* **1966**, 32, 689.
- [2] T. Irie, K. Takaki, I. Tsutsunaga, Y. Sano, *Tetsu-to-Hagane* **1979**, 65, 293.
- [3] J. H. Lee, J. C. Oh, J. W. Park, H. C. Lee, S. Lee, *ISIJ Int.* **2001**, 41, 859.
- [4] M. Sedlaček, B. Podgornik, S. Milanovic, *Mater. Technol.* **2014**, 48, 983.
- [5] N.-A. Noda, K. Hu, Y. Sano, Y. Hosokawa, X. Wang, *ISIJ Int.* **2017**, 57, 1432.
- [6] S. Tutumi, S. Hara, S. Yoshi, *Tetsu-to-Hagane* **1971**, 57, 818.
- [7] S. Spuzic, K. N. Strafford, C. Subramanian, G. Savage, *Wear* **1994**, 176, 261.
- [8] Z. H. Guo, F. Xiao, S. Lu, H. Li, B. Liao, *Adv. Mater. Sci. Eng.* **2016**, 2016, 1.
- [9] N.-A. Noda, Y. Sano, Y. Takase, Y. Shimoda, G. Zhang, *J. Jpn Soc. Technol. Plasticity* **2017**, 58, 66.
- [10] K. Hu, Y. Xia, F. Zhu, N.-A. Noda, *Steel Res. Int.* **2018**, 89, 1.

- [11] N.-A. Noda, H. Sakai, Y. Sano, Y. Takase, Y. Shimoda, *Metals* **2018**, *8*, 998.
- [12] H. Sakai, N.-A. Noda, Y. Sano, G. Zhang, Y. Takase, *Tetsu-to-Hagane* **2019**, *105*, 1126.
- [13] H. Sakai, N.-A. Noda, Y. Sano, G. Zhang, Y. Takase, *ISIJ Int.* **2019**, *9*, 889.
- [14] K. Goto, Y. Matsuda, K. Sakamoto, Y. Sugimoto, *ISIJ Int.* **1992**, *32*, 1184.
- [15] J. H. Ryu, H. B. Ryu, *ISIJ Int.* **2003**, *43*, 1036.
- [16] J. W. Park, H. C. Lee, S. Lee, *Metall. Mater. Trans. A* **1999**, *30*, 399.
- [17] Y. Sano, T. Hattori, M. Haga, *ISIJ Int.* **1992**, *32*, 1194.
- [18] H. Fu, Q. Xiao, J. D. Xing, *Mater. Sci. Eng. A* **2008**, *474*, 82.
- [19] Y. Sano, in *The 245th JSMS Committee on Fatigue of Materials and The 36th JSMS Committee on Strength Design Safety Evaluation*, The Society of Materials Science Japan, Kyoto, Japan **1999**, p. 40.
- [20] Y. Sano, K. Kimura, *Tetsu-to-Hagane* **1987**, *73*, 1154.
- [21] H. Li, Z. Jiang, K. A. Tieu, W. Sun, *Wear* **2007**, *263*, 1442.
- [22] G. Pantazopoulos, A. Vazdirvanidis, *J. Fail. Anal. Prev.* **2008**, *8*, 509.
- [23] M. A. Tolcha, H. Altenbach, G. S. Tibba, *Fatigue Fract. Eng. M.* **2019**, *42*, 2611.
- [24] Q. Dong, J.-G. Cao, H.-B. Li, Y.-S. Zhou, T.-L. Yan, W.-Z. Wang, *Steel Res. Int.* **2015**, *86*, 129.
- [25] Y. Ohkumori, C. Sakae, Y. Murakami, *J. Soc. Mater. Sci., Japan* **2001**, *50*, 249.
- [26] Y. Ohkumori, I. Kitagawa, K. Shinozuka, R. Miyamoto, S. Yazaki, M. Inoue, *Tetsu-to-Hagane* **2009**, *73*, 691.
- [27] J.-G. Cao, Y.-P. Wang, N. Kong, L.-H. Yang, A.-Q. Hou, Z.-B. Wang, *Engineering Mechanics* **2011**, *28*, 194.
- [28] N. Kong, J.-G. Cao, Y.-P. Wang, A. K. Tieu, L.-H. Yang, A.-Q. Hou, Z.-B. Wang, *Mater.* **2014**, *29*, 129.
- [29] M. Drobne, U. Klannik, P. Fajfar, M. Terelj, *J. Mater.* **2021**, *12*, 186.
- [30] N.-A. Noda, K. Hu, Y. Sano, K. Ono, Y. Hosokawa, *Steel Res. Int.* **2016**, *87*, 1478.
- [31] N.-A. Noda, K. Hu, Y. Sano, K. Ono, Y. Hosokawa, *Steel Res. Int.* **2017**, *88*, 1600165.
- [32] N.-A. Noda, Y. Sano, M. R. Aridi, K. Tsuboi, N. Oda, *Metals* **2018**, *8*, 952.
- [33] N.-A. Noda, M. R. Aridi, R. Torigoe, K. Tsuboi, Y. Sano, *J. Jpn Soc. Technol. Plast.* **2020**, *61*, 183.
- [34] Y. Sano, in *The 93rd Lecture on Technology of Plasticity*, The Japan Society for Technology of Plasticity, Nagoya, Japan **2004**, p. 199.
- [35] H. Sakai, N.-A. Noda, Y. Sano, G. Zhang, Y. Takase, *Tetsu-to-Hagane* **2019**, *105*, 1126.
- [36] The Iron and Steel Institute of Japan, *Recent Hot Strip Manufacturing Technology in Japan*, The Iron and Steel Institute of Japan, Tokyo, Japan **1987**.
- [37] Z. Y. Jiang, D. Wei, A. K. Tieu, *J. Mater. Process. Technol.* **2009**, *209*, 4584.
- [38] J.-G. Cao, G.-C. Wei, J. Zhang, X.-L. Chen, Y.-Z. Zhou, *J. Cent. South Univ.* **2008**, *15*, 264.
- [39] N. T. Zhao, J.-G. Cao, J. Zhang, Y. Su, T.-L. Yan, K.-F. Rao, *J. Univ. Sci. Technol. Beijing* **2008**, *15*, 352.
- [40] J.-G. Cao, S. J. Liu, J. Zhang, P. Song, T.-L. Yan, Y.-Z. Zhou, *J. Mater.* **2011**, *211*, 1768.
- [41] X.-T. Li, M.-T. Wang, F.-S. Du, G.-L. Zhang, *J. Cent. South Univ.* **2014**, *21*, 2160.
- [42] F. J. Belzunce, A. Ziadi, C. Rodriguez, *Eng. Fail. Anal.* **2004**, *11*, 789.
- [43] Y. Sekimoto, K. Tanaka, K. Nakajima, T. Kawanami, *Tetsu-to-Hagane* **1975**, *61*, 2337.
- [44] Y. Sekimoto, *J. Jpn Soc. Technol. Plast.* **1982**, *23*, 953.
- [45] C. S. Li, H. L. Yu, G. Y. Deng, X. H. Liu, G. D. Wang, *J. Iron Steel Res. Int.* **2007**, *14*, 18.
- [46] S. Hamada, Y. Sakoda, D. Sasaki, M. Ueda, H. Noguchi, *Soc. Mater. Sci.*, **2011**, *9*, 790.
- [47] A. A. Garcia-Granada, D. J. Smith, M. J. Pavier, *Int. J. Mech. Sci.*, **2000**, *42*, 1027.
- [48] K. Kamimiyada, Y. Konno, A. Yanagitsuru, *Mater. Trans.* **2020**, *61*, 1987.
- [49] N. A. Noda, K. Hu, Y. Sano, Y. Hosokawa, X. Wang, *ISIJ Int.* **2017**, *57*, 1432.
- [50] G. Luo, Y. Liu, *Mar. Struct.* **2018**, *58*, 367.
- [51] T. Sakai, B. Lian, M. Takeda, K. Shiozawa, N. Oguma, Y. Ochi, M. Nakajima, T. Nakamura, *Int. J. Fatigue* **2010**, *32*, 497.
- [52] E. Zalnezhad, A. A. D. Sarhan, P. Jahanshahi, *Int. J. Adv. Manuf. Technol.* **2014**, *70*, 2211.
- [53] K. H. Schroder, *A Basic Understanding Of The Mechanics Of Rolling Mill Rolls*, Eisenwerk Sulzau-Werfen, ESW-Handbook, Tenneck, Austria **2003**.
- [54] H. Nisitani, N. Yamashita, *Trans. JSME* **1966**, *32*, 1456.
- [55] H. Nisitani, M. Goto, *Trans. JSME Part A* **1984**, *50*, 1926.
- [56] Y. Akiwaka, K. Tanaka, N. Taniguchi, *Trans. JSME Part A* **1987**, *53*, 1768.
- [57] A. Ince, G. Glinka, *Fatigue Fract. Engng. Mater. Struct.* **2011**, *34*, 854.
- [58] K. Kasaba, T. Sano, S. Kudo, T. Shoji, K. Katagiri, T. Sato, *J. Nucl. Mater.* **1998**, *258–263*, 2059.
- [59] T. Hidaka, N.-A. Noda, Y. Sano, N. Kai, H. Fujimoto, *ISIJ Int.* **2019**, *59*, 1860.
- [60] T. Hidaka, N.-A. Noda, Y. Sano, N. Kai, H. Fujimoto, *ISIJ Int.* **2020**, *60*, 1006.
- [61] Y. Murakami, *Metal Fatigue: Effect of Small Defects and Nonmetallic Inclusions*, Elsevier Science, Kidlington, Oxford, UK **2002**.